

A Component of the Smith High Velocity Cloud Now Crossing the Galactic Plane

FELIX J. LOCKMAN ¹, ROBERT A. BENJAMIN ², NICOLAS PICHETTE ³ AND CHRISTOPHER THIBODEAU ^{4, *}

¹*Green Bank Observatory, Green Bank, WV 24944, USA*

²*Dept. of Physics, University of Wisconsin-Whitewater, Whitewater, WI 53190*

³*Dept. of Physics, Montana State University, Bozeman, MT*

⁴*Department of Physics, Astronomy & Geosciences, Towson University, Towson, MD.*

ABSTRACT

We have identified a new structure in the Milky Way: a leading component of the Smith high velocity cloud that is now crossing the Galactic plane near longitude 25° . Using new 21cm HI data from the Green Bank Telescope (GBT) we measured the properties of several dozen clouds that are part of this structure. Their kinematics is consistent with that of the Smith Cloud with a V_{LSR} exceeding that permitted by circular rotation in their direction. Most of the clouds in the Leading Component show evidence that they are interacting with disk gas allowing the location of the interaction to be estimated. The Leading Component crosses the Galactic plane at a distance from the Sun of 9.5 kpc, about 4.5 kpc from the Galactic Center. Its HI mass may be as high as $10^6 M_\odot$, comparable to the mass of the neutral component of the Smith Cloud, but only a fraction of this is contained in clouds that are resolved in the GBT data. Like the Smith Cloud, the Leading Component appears to be adding mass and angular momentum to the ISM in the inner Galaxy. We suggest that the Smith Cloud is not an isolated object, but rather part of a structure that stretches more than 40° (~ 7 kpc) across the sky, in two pieces separated by a gap of ~ 1 kpc.

Keywords: ISM: clouds – ISM: individual objects (Smith Cloud) – Galaxy: structure – Galaxy: evolution

1. INTRODUCTION

The old puzzle of the Milky Way’s high velocity clouds – those aggregations of neutral and ionized gas whose velocities deviate significantly from that allowed by Galactic rotation – continues to confound and delight. The origin of most high velocity clouds (HVCs) is uncertain. Because the category is defined solely on kinematics (e.g., Wakker & van Woerden 1991), it can encompass everything from gas stripped from satellite galaxies, accretion from the intergalactic and circumgalactic medium, and material recycled from the Galactic disk (Oort 1969; Wakker & van Woerden 1997; Marinacci et al. 2010; Binney & Fraternali 2012; Putman et al. 2012). HVCs cover a large fraction of the sky (Lockman et al. 2002; Lehner et al. 2022). The large HVC complexes lie in the Galactic halo and are typically found within 10 kpc of the Galactic plane (Putman 2017). HVCs have now been detected in other galaxies, e.g., M31 (Braun & Thilker 2004; Thilker et al. 2004; Westmeier et al. 2008; Wolfe et al. 2016), though not with the sensitivity and richness of detail available to studies of the Milky Way.

HVCs are important in understanding the evolution of galaxies as they can be manifestations of both gas accretion and recycling from a galactic fountain (Putman 2017; Richter 2017; Fraternali 2017; Li & Tonnesen 2020). A number of HVCs have a cometary or head-tail morphology or other indications that they are interacting with an external medium (Putman et al. 2011; Barger et al. 2020). There is also evidence for the interaction of infalling HVCs with neutral gas in the Galactic plane (Lockman 2003; McClure-Griffiths et al. 2008; Park et al. 2016). These clouds must have survived their passage through the halo to merge with the Milky Way disk.

Corresponding author: F. J. Lockman
jlockman@nrao.edu

* Current Address: 236 Braeden Brooke Dr. San Marcos, TX 78666

The Smith Cloud is one of the most prominent high-velocity clouds; it was discovered even before the identification of HVCs as a class of interstellar object (Smith 1963; Muller et al. 1963). In neutral hydrogen emission the Smith Cloud extends over more than 10° on the sky with a highly-organized cometary shape. It has a magnetic field draped around it (Hill et al. 2013; Betti et al. 2019). The Cloud contains at least $10^6 M_\odot$ of HI and probably an equal mass in ionized gas but has no prominent stellar counterpart (Lockman et al. 2008; Hill et al. 2009; Stark et al. 2015). Its metallicity has been determined through optical emission and UV absorption spectroscopy to be approximately half Solar (Hill et al. 2009; Fox et al. 2016), but this may reflect more the medium with which it has exchanged material than any initial property of the cloud (Gritton et al. 2014; Henley et al. 2017; Heitsch et al. 2022). The distance to the Smith Cloud derived from three different methods is 12.4 kpc, placing it 2.9 kpc below the Galactic Plane (Putman et al. 2003; Wakker et al. 2008; Lockman et al. 2008). The kinematics of the cloud has been analyzed by Lockman et al. (2008, hereafter L08) who suggest that it is on a course to collide with the Milky Way disk in ≈ 30 Myr, adding mass and angular momentum to the Galaxy, and possibly triggering a burst of star formation (Alig et al. 2018). The Smith Cloud has been modelled as the gas remnant of a dwarf galaxy merging with the Milky Way (Bland-Hawthorn et al. 1998), the baryonic component of a dark matter subhalo (Nichols & Bland-Hawthorn 2009; Nichols et al. 2014; Tepper-García & Bland-Hawthorn 2018), and the product of supernove or the Galactic fountain (Sofue et al. 2004; Marasco & Fraternali 2017).

This is the first in a series of papers exploring aspects of the Smith Cloud. Future papers will report on studies of its structure, interaction with the circumgalactic medium, molecular content, and trajectory. Here we describe a major interstellar feature associated with the Smith Cloud: a leading component that is now passing through the Galactic disk.

HVCs are easily detected at high Galactic latitude where their discrepant velocities stand out most clearly from Galactic disk gas. There is no reason to believe, however, that the phenomenon is not widespread, and that a significant fraction of the HVC population has been missed through confusion with gas at permitted velocities (Zheng et al. 2015). Indeed, distinctions based solely on velocity certainly give a biased view of phenomena in the Galactic halo (Bish et al. 2021; Marasco et al. 2022).

In a search for potential HVCs at low Galactic latitude, we constructed a slice through the LAB HI survey (Kalberla et al. 2005) in the first Galactic quadrant, integrating over a velocity interval $15\text{--}35 \text{ km s}^{-1}$ greater than expected for circular Galactic rotation for a reasonable Galactic rotation curve. In the inner Galaxy, the maximum value of $|V_{\text{LSR}}|$ from circular rotation occurs at the tangent point, where the distance from the Sun, r , is $R_0 \cos(\ell)$, and R_0 is the distance to the Galactic Center. By sampling emission from velocities slightly greater than allowed by circular rotation we are measuring gas in the line wing, which in the absence of non-circular motions should arise from regions close to the tangent point. In this instance we used the rotation curve function given by Brand & Blitz (1993) with coefficients from Burton (1988), although as we will show, the basic findings are not sensitive to details of the adopted rotation curve. The results over a $40^\circ \times 40^\circ$ region are shown in Figure 1.

The HI emission visible in this figure arises from three separate sources. First, because of temperature and turbulence there will always be some emission in the line wings at velocities extending beyond that allowed by Galactic rotation. The amount of emission in the line wings depends on the velocity dispersion of the gas, but also on $|dV_{\text{LSR}}/dr|^{-1}$ – often called velocity crowding – which is the degree to which the velocity of gas at different distances from the Sun, r , projects to a difference in V_{LSR} (Burton 1971; Celnik et al. 1979). The sense of this geometric effect is that V_{LSR} changes more slowly with distance at high longitudes than at low longitudes, so more emission appears in line wings at a forbidden velocity at $\ell = 50^\circ$ than at $\ell = 30^\circ$. The dashed yellow lines above and below latitude 0° in Figure 1 mark a distance ± 0.25 kpc from the plane at the tangent points and outline expectations for the contribution from line wings and velocity crowding.

A second factor affecting the appearance of Figure 1 is large-scale streaming motions that arise from, for example, gas response to spiral arms (Burton 1971). Although these are easily detected in the data (e.g., Fig. 8 in McClure-Griffiths & Dickey (2007) and Figs. 6 and 7 in Levine et al. (2008)), they are not included in rotation curves that describe only the symmetric component. Large-scale streaming contributes to the emission observed in Figure 1 around longitude 32° and 50° . Note that both turbulence and streaming motions are expected to be approximately symmetric around the Galactic Plane, and that is what is observed.

But Figure 1 also shows emission not related to Galactic rotation in any sense. The Smith HVC dominates latitudes $b \lesssim -10^\circ$ between longitudes $35^\circ \leq \ell \leq 50^\circ$, and there is a component in HI emission almost as extensive as the Smith Cloud that lies along its axis but extends through the Galactic plane, crossing it around longitude $\ell = 25^\circ$. A dashed

cyan line connects these two features, which are clearly not symmetric about the Galactic Plane. The existence of a band of emission at forbidden velocity, aligned with the Smith Cloud, suggests that both may be part of a larger structure that shares a common kinematic anomaly. Because the morphology of the Smith Cloud indicates that its space motion is towards lower longitude and more positive latitude (L08), i.e., to the upper right in Figure 1, we call the component that extends through the Galactic plane the “Leading Component”. To understand its properties more fully we analyze new 21cm HI observations from the Green Bank Telescope (GBT) made over a large region for another purpose, and here present those data and the results.

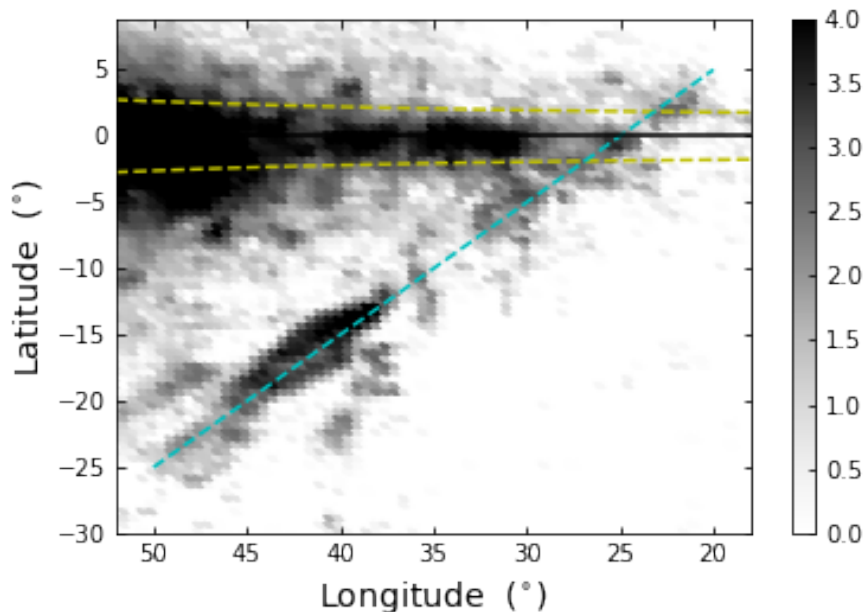


Figure 1. Map of the integrated HI brightness temperature along a slice through the LAB survey that includes only emission between 15 and 35 km s^{-1} in excess of that allowed by circular Galactic rotation. Dashed yellow lines mark a distance $z = \pm 0.25$ kpc from the plane at the tangent point distance of each longitude. Normal thermal and turbulent motions, along with velocity crowding, will produce forbidden-velocity emission in this range whose brightness is expected to increase to higher longitude over areas approximately bound by curves of constant $|z|$. The Smith Cloud is in the lower left between longitudes $40^\circ \lesssim \ell \lesssim 50^\circ$ centered around latitude $b \approx -15^\circ$. This Figure shows that there is also emission that extends through the Galactic plane along the axis of the Cloud, marked by the diagonal dashed cyan line. We call this the Leading Component. The grey scale is proportional to the square root of the integrated HI brightness temperature.

In section 2 the new GBT HI survey is described, as well as an existing study that provides high resolution images of several clouds in the Leading Component. A catalog of HI clouds found in the Leading Component is presented in section 3 along with a discussion of their general properties. Section 4 discusses evidence that some of these leading clouds are interacting with normally rotating disk gas, allowing derivation of a kinematic distance. Their overall space velocity is analyzed in section 5, which is followed by a discussion of the implications of the present work.

2. OBSERVATIONS

2.1. The GBT HI Survey

Measurements of the 21cm line of HI were made with the Green Bank Telescope (GBT) using the standard L band receiver and the GBT spectrometer (Prestage et al. 2009). Data were taken “on-the-fly” using in-band frequency switching and were calibrated as described in Boothroyd et al. (2011). A low order polynomial was fit to emission-free regions of the spectra after they were gridded into a cube with a channel spacing of 0.80 km s^{-1} over a velocity range of $-200 \leq V_{\text{LSR}} \leq +275 \text{ km s}^{-1}$. The data cover $13^\circ \leq \ell \leq 35^\circ$ over a latitude range $\pm 10^\circ$ with a partial extension to latitude -14° at $\ell \geq 30^\circ$ to include the tip of the Smith Cloud. The effective angular resolution is $10'$. The median rms noise in brightness temperature for a 1 km s^{-1} channel is 0.12 K. The noise varies somewhat across the mapped area,

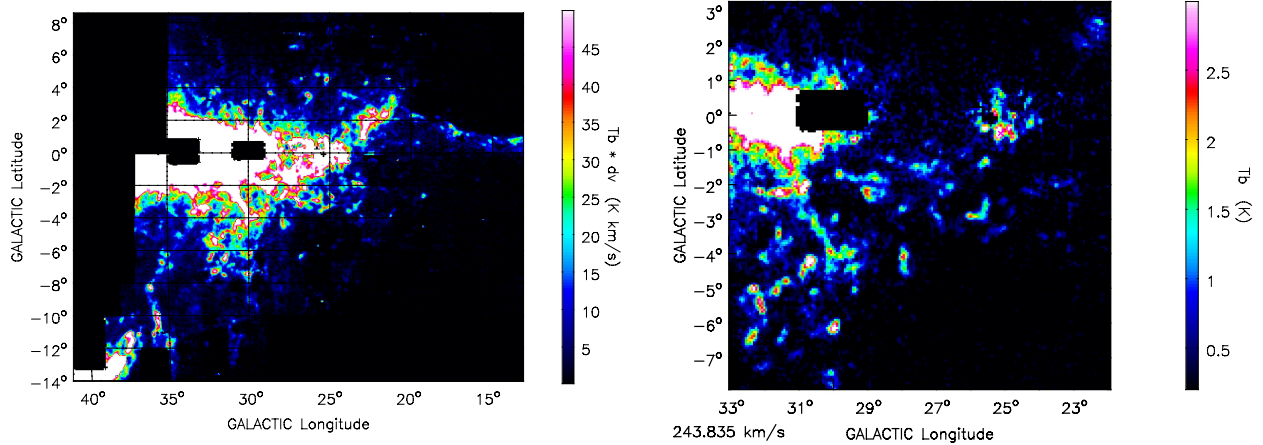


Figure 2. Longitude-latitude maps from the new GBT HI survey. Coverage is almost complete over $13^\circ \leq \ell \leq 35^\circ$ and $-10^\circ \leq b \leq +10^\circ$. The new data show the tip of the Smith Cloud in the lower left of the left panel. The Leading Component stands out as a band of emission with the same position angle as the Smith Cloud, extending from $(\ell, b) = (32^\circ, -7^\circ)$ to $(22^\circ, +4^\circ)$. Black rectangles mark areas blanked in the GBT data. *Left Panel:* The integrated HI emission over $+226 \leq V_{\text{GSR}} \leq +275 \text{ km s}^{-1}$. *Right Panel:* Channel map at $V_{\text{GSR}} = 243.8 \text{ km s}^{-1}$ over the central region of the GBT survey. Here we see that some of the Leading Component is resolved into individual clouds.

being greatest within 2° of the Galactic plane where there was often a significant increase in the system temperature from continuum emission. A small fraction of the mapped area had to be blanked over regions of strong continuum emission or because of occasional radio frequency interference.

For study of the Leading Component, the new data have a distinct advantage over the premier existing HI survey, HI4PI (HI4PI Collaboration et al. 2016). Emission from the leading component is not particularly faint, so although HI4PI has about one-third lower noise level than the new GBT data, noise is not a critical factor. The $10'$ angular resolution of the GBT data compared with the $16.2'$ of HI4PI is, however, important in sorting out confusion between the leading component and other HI emission. Virtually all of the Leading Component lies at J2000 declination $\delta < -5^\circ$, which is outside the declination limit of any survey using the Arecibo telescope.

The new GBT survey is shown in Figure 2 as emission integrated over forbidden velocities (left), i.e., those velocities not permitted by circular Galactic rotation, and as a map of emission in a single velocity channel (right). The left panel shows the tip of the Smith Cloud at the lower left and the Leading Component in the center of the Figure. The velocity with respect to the Local Standard of Rest, V_{LSR} , is not appropriate for the study of objects that cover a large angle on the sky, as the changing projection of the LSR across the structure becomes significant. A more suitable measure is the velocity with respect to the Galactic Standard of Rest defined as $V_{\text{GSR}} = V_{\text{LSR}} + |V_0| \sin(\ell) \cos(b)$, where V_0 is the circular velocity of Galactic Rotation at the Sun's distance from the Galactic Center, R_0 . Throughout this paper we use $R_0 = 8.1 \text{ kpc}$ and $V_0 = 230 \text{ km s}^{-1}$, consistent with the results of recent studies (Gravity Collaboration et al. 2018; Eilers et al. 2019). The right panel of Figure 2 is a channel map over the central part of the new GBT survey at a constant V_{GSR} of 243.8 km s^{-1} , showing that the Leading Component contains discrete clouds.

2.2. High Angular Resolution Measurements

Pidopryhora et al. (2015, hereafter P2015) combined GBT and VLA data to produce HI maps of 10 interstellar clouds at $\sim 1'$ angular resolution, corresponding to a linear resolution of 3 pc at a distance of 10 kpc. The clouds cover a range of longitude ($16^\circ 0' \leq \ell \leq 44^\circ 8'$) and latitude ($-8^\circ 7' \leq b \leq +4^\circ 5'$). The sample was selected to have

little confusion with other neutral HI, so these clouds are somewhat outside of the Galactic plane (median $|b| = 4.9^\circ$) and have a velocity beyond the terminal velocity ($V_{\text{LSR}} \geq V_t$), where the terminal velocity is the maximum permitted by Galactic rotation in their direction. Three of the P2015 clouds turn out to be clouds in the Leading Component. Although the noise in the P2015 data is about three times worse than the GBT data (approximately 0.36 K in a 1 km s^{-1} channel) its much higher angular resolution reveals important structure within the clouds.

3. LEADING CLOUDS

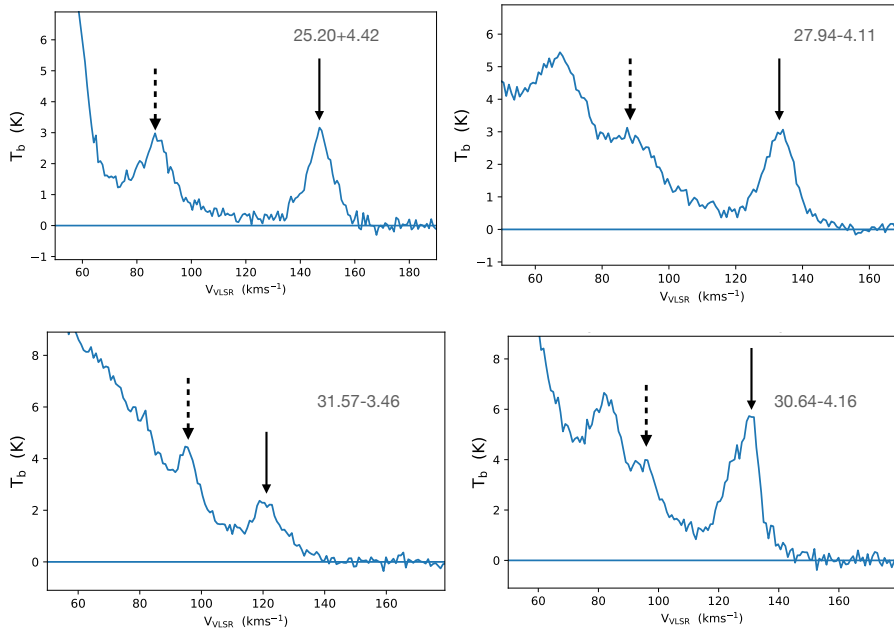


Figure 3. GBT HI spectra showing examples of the clouds detected in this survey associated with the Leading Component of the Smith Cloud identified by their ℓ, b coordinates. The leading cloud is always the highest velocity spectral feature, marked with the solid arrow. All these clouds appear to be interacting with a component of disk gas at a lower (permitted) velocity, marked with a dashed arrow. This is discussed in more detail in [section 4](#).

3.1. Cloud Properties

At the angular resolution of the GBT data the Leading Component contains a number of individual clouds many of which are isolated in ℓ, b , and velocity, so that their properties can be measured accurately. The right panel of [Figure 2](#) shows a region of the survey centered near $(\ell, b) = (27^\circ, -2^\circ)$ in which a number of individual clouds can be identified. The clouds lie in a swath that begins a few degrees above the top of the Smith Cloud around $(\ell, b) = (35^\circ, -8^\circ)$ and extends at least to $b > +4^\circ$ at $\ell < 24^\circ$. Discrete clouds associated with the leading component were identified using three criteria: 1) a location on or near the main region of the leading component; 2) a V_{LSR} that was close to or beyond that permitted by circular Galactic rotation in their direction; and, 3) for most of the clouds, evidence that they were interacting with gas at a lower, permitted velocity. Spectra towards 4 of the leading clouds are shown in [Figure 3](#). They are detected well above the noise in the GBT data.

There are also cloud-like structures visible in channel maps whose spectral components cannot be separated from lower velocity emission. This is especially common close to the Galactic plane. Examples are shown in [Figure 4](#). These are not included in [Table 1](#).

Clouds were identified in channel maps and a Gaussian was fit to the spectrum at the location of the peak N_{HI} . A 2-d Gaussian model was used to derive an angular size and position angle. HI masses were measured by integrating

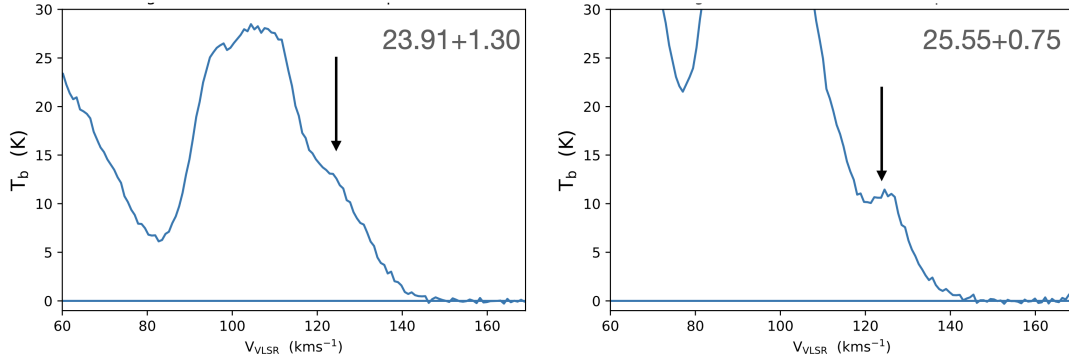


Figure 4. GBT HI spectra of Leading Component clouds that are confused with lower velocity emission (arrows). The longitude and latitude is indicated in each panel. These spectral features are distinct clouds in channel maps and have a V_{LSR} exceeding that permitted by Galactic rotation, but cannot be separated from lower velocity emission and, like others with similar properties, are therefore not included in Table 1.

over an area of the channel map encompassing the measurable extent of the cloud at the velocity of the HI peak. Background HI emission was estimated from measurements around the edge of the cloud and subtracted. The result was then multiplied by the FWHM of the line at the brightest location to obtain a line power integrated over area and velocity. Some clouds were so confused with other emission that it was not possible to measure their size.

Properties of 38 clouds are given in Table 1. We emphasize that the sample of clouds presented here does not completely account for all the clouds or all the HI mass in the leading component; it represents only the more easily-identifiable and less-confused clouds in the GBT data. The longitude and latitude of the peak HI brightness is in the first two columns, and quantities in cols. 3 through 6 refer to that location. Errors in line parameters were derived from the Gaussian fit to the spectrum. The median peak T_b of the clouds is 2.5 K which is a detection at the 20σ level above the noise. The faintest cloud is detected at 6.5σ . The angular size in col. 7 is not corrected for beam smearing. The position angle is measured counter-clockwise with reference to the Galactic North Pole such that a cloud elongated parallel to the Galactic plane would have $\text{PA} = 90^\circ$. For the purposes of calculating general cloud properties we assume that they are all at a distance $d_{10} = 10$ kpc. This is comparable to the distance of the Smith Cloud, 12.4 kpc (L08), and results can be scaled easily. The distance of the Leading Component is discussed further in section 4.

Properties of the leading cloud population are summarized in Table 2.

The measured angular size of the clouds, Θ_{obs} , was corrected for beam convolution by subtracting the $10'$ resolution of the data cube in quadrature from the measured Θ_{maj} and Θ_{min} . Cloud diameters were derived from the square root of the product of the major and minor deconvolved angular sizes, at a distance of 10 kpc. They are shown in the upper right panel of Figure 5.

The cloud HI mass distribution is shown in Figure 5 for an assumed distance of 10 kpc. The sum of the HI mass of the tabulated clouds is $1.1 \times 10^5 M_\odot$. The HI mass in the entire leading component was estimated by summing over a large region encompassing the leading component, and integrating over all $V_{\text{GSR}} \geq 226 \text{ km s}^{-1}$. The result, $8 \times 10^5 M_\odot$ for a distance of 10 kpc, has a large uncertainty, but implies that the tabulated clouds contain only a small fraction ($\sim 15\%$) of the total HI associated with the system.

A lower limit to the volume density of the clouds can be derived from the ratio of the peak column density, N_{HI} , to the cloud diameter. This is a lower limit because the observed N_{HI} is certainly reduced to some extent by beam convolution, while this effect was taken out, at least approximately, in calculating the diameter.

The distribution of cloud position angles is shown in the bottom panel of Figure 5, where to avoid artificial discontinuities at 180° each cloud is counted twice, once at its PA and once at its $\text{PA}+180^\circ$. The distribution peaks around the PA of the Smith Cloud, which is also the PA of the Leading Component, 130° , suggesting that some individual clouds are being shaped by the same interaction with their environment as the Smith Cloud itself.

3.2. Comparison with higher angular resolution observations

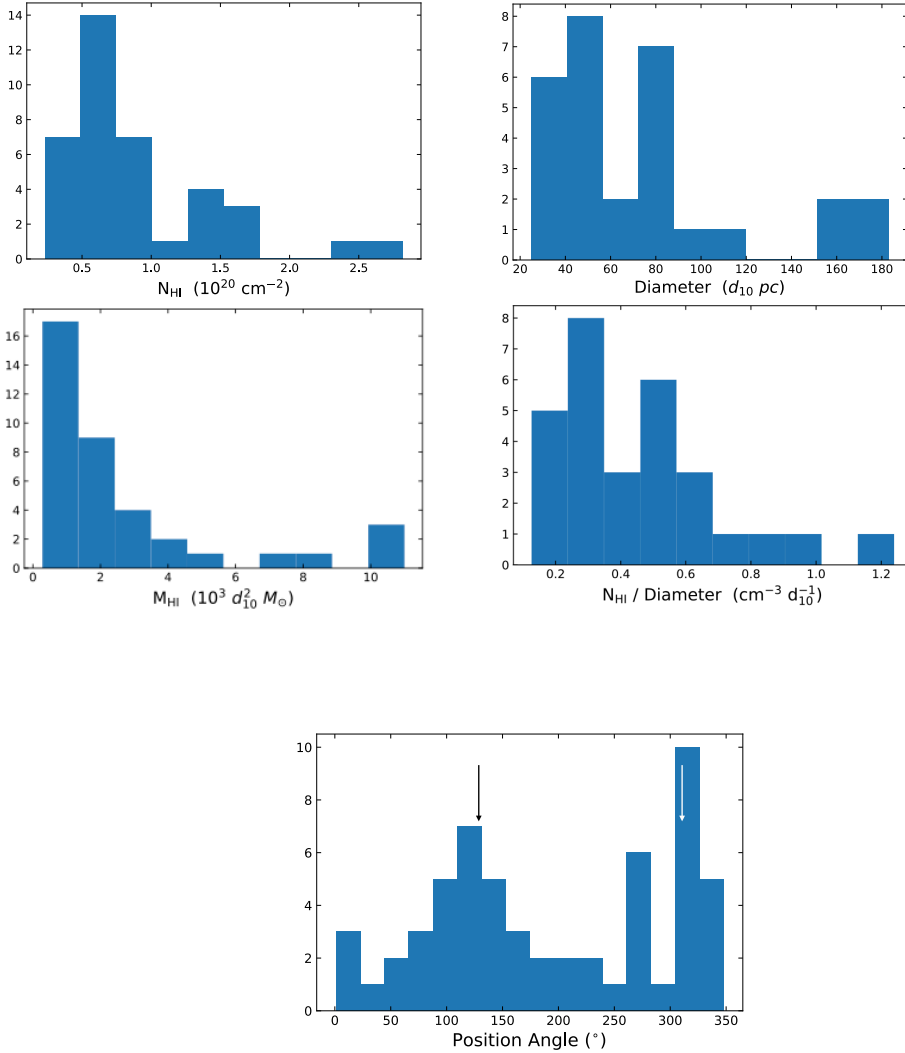


Figure 5. Properties of the leading clouds. *Top left:* N_{HI} measured at the position of peak line brightness assuming optically thin emission. *Top right:* Cloud diameter deconvolved for beam smearing assuming a 10 kpc distance. *Center left:* HI mass of the leading clouds assuming a distance of 10 kpc. The median $M_{\text{HI}} = 1.6 \times 10^3 (d_{10}^2) M_{\odot}$. *Center right:* Estimate of the average volume density in the clouds from the ratio of the peak column density to the diameter. The diameter is corrected for beam convolution and scaled to a distance $d_{10} = 10$ kpc. The median $n_{\text{HI}} = 0.43 \text{ cm}^{-3}$. *Bottom:* Distribution of position angles for the leading clouds. Each cloud is displayed twice, once at its PA and once at its PA+180°. The two vertical arrows mark the PA of the Smith Cloud, 130°. The data suggest that many individual clouds share the same elongation as the Smith Cloud.

Three of the leading clouds from Table 1 were observed in the P2015 survey and we can compare properties derived from GBT data with those from the higher angular resolution data. The results are given in Table 3, where P2015 diameters have been scaled to a distance of 10 kpc. Velocities are in good agreement, while the higher angular resolution of P2015 gives larger peak values of N_{HI} by a factor of 2 - 3. The higher resolution data often reveal cloud cores with a diameter less than one-third that given by the GBT data. The increase in peak N_{HI} and smaller cloud core size combine to increase the central cloud density by factors of more than six. It is interesting that these clouds

are elongated along the direction of the Leading Component axis, with position angles clustered around the 130° PA of the Smith Cloud.

3.3. Leading Cloud Kinematics

Values of V_{LSR} and V_{GSR} for the clouds are shown in a position-velocity diagram in Figure 6. The solid line is at the median V_{GSR} of the sample, 237 km s^{-1} , while the mean V_{GSR} is identical at $237.1 \pm 6.8 \text{ km s}^{-1} (1\sigma)$. The V_{GSR} of the central region of the Smith Cloud, marked by the dashed line, is essentially identical to that of the leading clouds at 241 km s^{-1} . The dotted line at 226 km s^{-1} marks the lower velocity limit of the integrated emission displayed in the left panel of Figure 2, which was used to estimate the HI mass of the entire Leading Component system.

As we will discuss in section 5, the quantity V_{GSR} is directly related to the total space velocity of an object. The combination of similar V_{GSR} and an apparent association on the sky strongly supports a physical connection between the Leading Component and the Smith Cloud.

From a rotation curve which gives $V_\theta(R)$, a terminal (maximum) velocity can be calculated for every longitude $|\ell| < 90^\circ$: $Vt \equiv \cos(b) [V_\theta(R_0)\sin(\ell) - V_\theta(R_t)]$, where $R_t = R_0 \sin(\ell)$. Each cloud can then be assigned a "forbidden" velocity, $V_{\text{for}} \equiv V_{\text{LSR}} - V_t$, which gives the amount by which the cloud's V_{LSR} is in excess of that allowed by circular Galactic rotation *at any location along that line of sight*.

We use two rotation curves: a flat rotation curve with $V_\theta(R) \equiv V_0 = 230 \text{ km s}^{-1}$, which is very close to the curve measured by Eilers et al. (2019) at $R \geq 5.27 \text{ kpc}$, and a "Universal" rotation curve (Persic et al. 1996) with coefficients from Mróz et al. (2019), that we call the PM model. The PM model differs from that of Reid et al. (2014) by only a few percent over the region of interest.

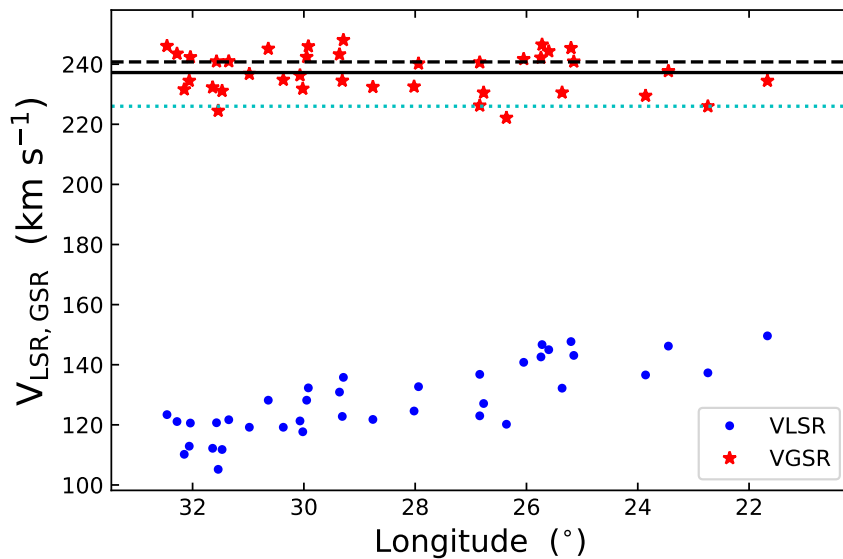


Figure 6. The leading clouds in position and velocity. The V_{LSR} (blue dots below) and V_{GSR} (red stars above) of the leading cloud sample is plotted vs. longitude. The solid horizontal line is the median V_{GSR} of the clouds, 237 km s^{-1} , while the dashed line is the V_{GSR} of the Smith Cloud, 241 km s^{-1} . There is no strong trend in V_{GSR} with longitude implying that the entire complex is consistent with having a single velocity vector projected to different values of V_{LSR} at different locations. The dotted line shows the lower limit to the V_{GSR} used in integrating over velocity to create the moment-zero map in the left panel of Figure 2.

Figure 7 shows the "forbidden velocities" V_{for} for the cloud sample plotted against longitude from the PM rotation curve on the left and the flat rotation curve on the right. The median value of V_{for} is 17.3 and 8.1 km s^{-1} , respectively. Forbidden velocities are larger in the PM model because, unlike the flat model, the PM rotational velocities decrease toward the Galactic Center reducing the maximum permitted V_{LSR} at lower longitudes. When analyzed with a flat rotation curve there are five clouds with $V_{\text{for}} \lesssim 0 \text{ km s}^{-1}$, but these all show signs of interaction with lower-velocity

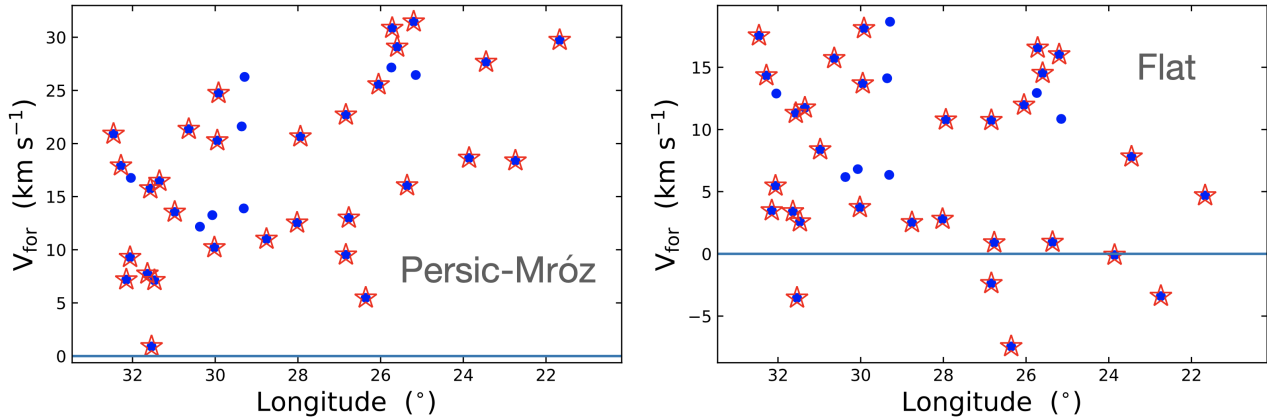


Figure 7. The “forbidden velocity” of the cloud sample, V_{for} , defined as the difference between a cloud’s V_{LSR} and the maximum permitted by circular Galactic rotation in their direction (blue dots). This is a lower limit to the peculiar line-of-sight velocity of a cloud. A more realistic estimate of a cloud’s deviation from circular rotation is given by the quantity V_{dif} , discussed in section 4. If the clouds show signs of interaction with lower velocity gas the points are overplotted with red stars. *Left panel:* Forbidden velocities evaluated for the Persic “Universal” rotation curve (Persic et al. 1996) with coefficients from Mróz et al. (2019). *Right Panel:* Forbidden velocities for a flat rotation curve at a circular velocity of 230 km s^{-1} . While there are 5 clouds with $V_{\text{for}} \lesssim 0$ for a flat rotation curve, values for the more realistic Persic curve, and evidence for interaction, suggests that they have anomalous velocities compared to their location in the Galaxy and are properly included in the leading cloud sample.

gas implying that they have a high non-circular velocity component (discussed in section 4). In Figure 7 clouds with evidence of interaction are marked with a red star.

4. INTERACTION WITH DISK GAS

Most of the clouds appear to be interacting with gas at lower V_{LSR} , i.e., with regularly rotating material in the Milky Way disc. In some cases the spectra show continuous emission between the velocity of the leading cloud and a lower-velocity component, overlapping in position with the cloud. The spectra in Figure 3 show four examples, where the lower velocity gas is marked with a dashed arrow. In many cases the connection is especially convincing, as illustrated in Figure 8. Here, in a display of latitude vs. V_{LSR} , we can see one or more edges of leading clouds forming a continuous bridge of HI emission to lower velocities, consistent with the outer regions of the clouds being stripped and decelerated. We compare Figure 8 to Figure 9 (from L08), which is a velocity-position cut through the minor axis of the Smith Cloud showing the same kinematic bridge between the anomalous velocity of the Smith Cloud and gas in the Milky Way disk.

The high-resolution P2015 data give additional information on the interaction for two leading clouds: G22.74+4.30 and G26.84-6.38 (we refer to these clouds by their GBT positions in Table 1, which deviate somewhat from the location of the brightest N_{HI} in the P2015 data). A map of total N_{HI} and a position-velocity cut through each cloud is shown in Figure 10. Unlike the clouds in Figure 8, these clouds do not exhibit kinematic bridges of material that join the cloud with lower-velocity gas, but in both cases there is a bright HI emission component centered approximately at the position of the leading cloud, but at a much lower velocity. The interaction between cloud and disk gas for G25.20+4.42 is shown more clearly in the GBT data of Figure 8 than in the P2015 data because the P2015 data do not have the sensitivity to detect the extended bridge of emission that connects this cloud kinematically to the disk.

It is interesting and perhaps significant that of the 10 clouds in the P2015 sample, only those three associated with the Leading Component show unambiguous evidence of interaction with gas at lower velocities.

In Table 1 the V_{LSR} of gas interacting with leading clouds is given as V_{MW} . This quantity is blank for clouds without identifiable interaction. The quantity V_{dif} , which is the difference in line-of-sight velocity between the cloud and the disk gas that it is encountering, $V_{\text{dif}} \equiv V_{\text{LSR}} - V_{\text{MW}}$, is shown in Figure 11.

The evidence for interaction provides two important pieces of information:

1. the leading clouds are in fact kinematically anomalous by a significant amount;
2. the velocity of the interacting gas might be used to derive a distance to the interaction.

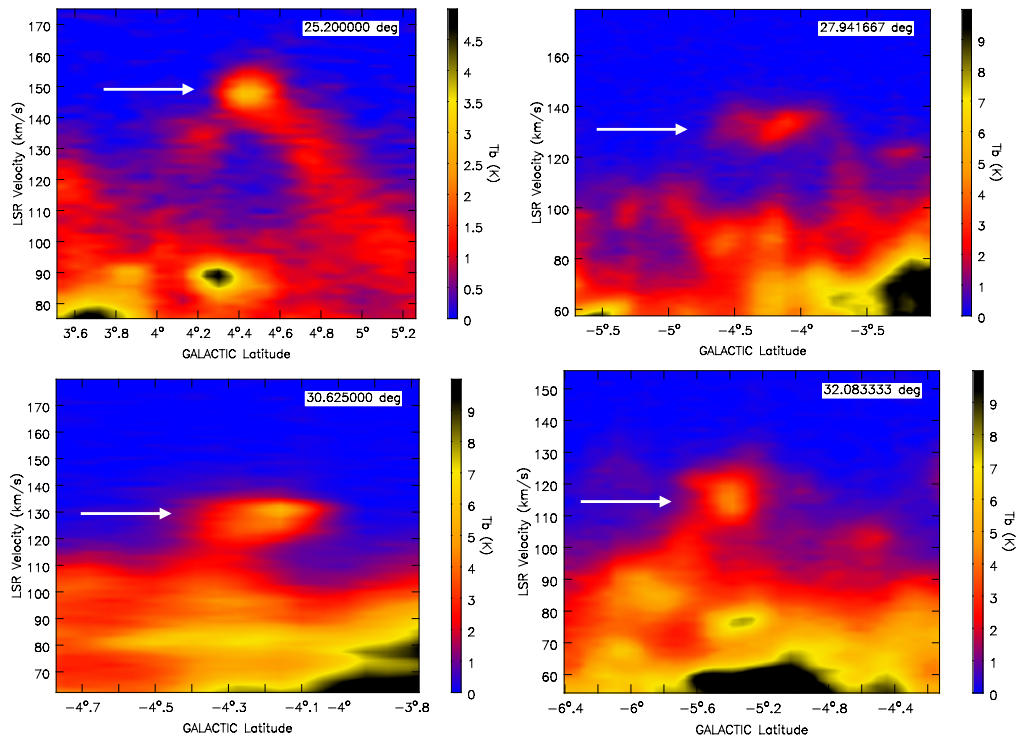


Figure 8. Examples of leading clouds showing their interaction with the Milky Way disk gas. In these latitude- V_{LSR} plots the leading cloud is always the feature at the highest velocity, marked with an arrow. There are “bridges” to lower velocity HI emission connecting these clouds to gas at a velocity consistent with normal Galactic rotation. This is often accompanied by an enhancement in the lower velocity emission. We interpret these figures as showing that these leading clouds are interacting with normal disk gas, with some cloud material being stripped away and decelerating to the lower, permitted velocity.

4.1. Location of the Interaction

We assume that the velocity of material apparently interacting with a leading cloud is in fact disk gas in circular rotation and thus can be used to identify the location of the interaction within the Galaxy. An identical line of argument was used for the Smith Cloud and produced a distance consistent with that derived from independent methods (L08). While there are many uncertainties in this approach, and the distance to any individual cloud may have a large error, this kinematic analysis has the potential to provide information on the location of the leading cloud population that is not otherwise available. In respect of the uncertainties in derived distances we do not discuss the location of individual clouds but rather limit our comments to properties of the ensemble. These do not vary greatly between the two rotation curves that were used.

We analyze the cloud interactions with the two rotation curves described earlier: a flat rotation curve with $V_{\theta}(R) = 230 \text{ km s}^{-1}$, and the PM “Universal” rotation curve (Persic et al. 1996; Mróz et al. 2019). For objects at the longitudes of the leading clouds, a given positive value of V_{LSR} occurs at a single value of R , the distance from the Galactic Center, but at two distances from the Sun. For the leading cloud sample the derived near distance is around 4 kpc, while the far distance is > 9 kpc. Given that the Smith Cloud is at a distance of 12.2 kpc we always choose the far kinematic distance for the leading clouds. The velocity of the interacting gas is rarely determined with high precision: to estimate an effect of this uncertainty on our results we evaluated the kinematic distances at the V_{LSR} of the interaction $\pm 5 \text{ km s}^{-1}$. In the few cases where a velocity is greater than permitted by the Galactic rotation model the tangent point distance is adopted as the most likely.

Figure 12 shows derived distances to the interacting gas and by inference, to the leading clouds themselves, using the PM rotation curve where the Sun is at $x = -R_0 = -8.1$ kpc. The interaction sites of the leading clouds cluster around median values of $x, y, z = 0.2, 4.5, -0.6$ kpc, at a median distance from the Sun of 9.5 kpc. This location is

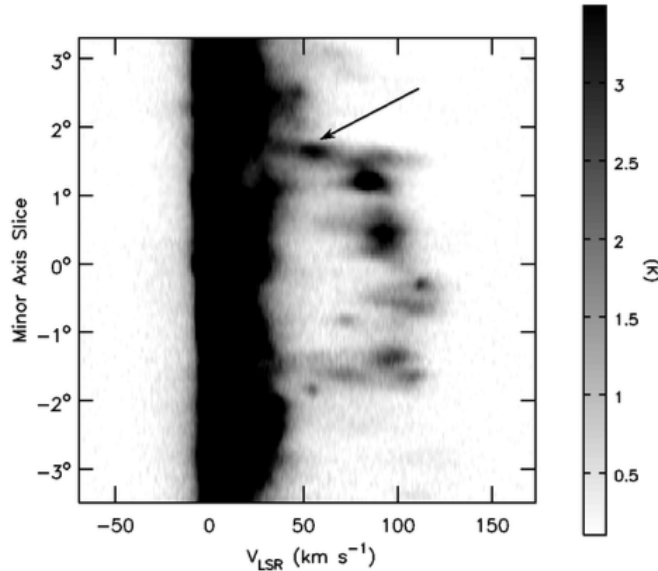


Figure 9. From Lockman et al. (2008), a position-velocity cut through the minor axis of the Smith Cloud, showing the same transition at the cloud edge between anomalous velocity gas and normally-rotating disk gas as is seen at the edges of the leading clouds of Figure 8. The arrow marks a small cloud that we interpret as having been detached from the Smith Cloud and decelerated by its interaction with the circumgalactic medium of the Milky Way.

more than 8 kpc away from the spot where the Smith Cloud is expected to cross the Galactic disk according to the trajectory of L08, marked with a black star on panel (c) of Figure 12.

4.2. Infall or Outflow?

Throughout this work we have assumed that the Smith Cloud and the Leading Component are manifestations of infall into the Milky Way. There have been suggestions, however, that the Smith Cloud results from a fountain process and is thus now moving away from the Galactic plane (Sofue et al. 2004; Marasco & Fraternali 2017). We believe that the properties of clouds in the Leading Component resolve this issue. For one, the Leading Component is found both above and below the Galactic plane at the same angle with respect to the plane as the Smith Cloud. This seems a very unlikely geometry for a supernova-driven superbubble originating in the Milky Way disk, but is unremarkable for an object passing through the Galactic plane. Second, some leading clouds have components that connect them to lower velocity emission, emission that is allowed by Galactic rotation (Figure 8). Were these clouds being accelerated outwards by a fast wind, the presumably stripped gas would be at a higher velocity. These considerations lead to the same conclusion when applied to the Smith Cloud itself (Figure 9). This discussion has no bearing on the origin of these objects, but the case for their infall at the current time is persuasive.

5. SPACE VELOCITY

In a right-handed cylindrical coordinate system centered on the Galactic center where the angle θ is measured from the Sun-center line such that $\ell \approx \theta$ at large distances, V_{GSR} can be written as the sum of three components, V_θ , V_R , and V_z

$$V_{\text{GSR}} = [-R_0 \sin(\ell) V_\theta / R + V_R \cos(\ell - \theta)] \cos(b) + V_z \sin(b) \quad (1)$$

where in this system the circular velocity $V_\theta < 0$.

There are two limiting cases of interest: first, near the Galactic Plane $\sin(b) \approx 0$, so vertical velocities do not contribute significantly to V_{GSR} . Second, at locations near the tangent points the quantity $\cos(\ell - \theta) \approx 0$, and the radial component of motion, V_R , does not contribute to V_{GSR} . At these locations V_{GSR} is a direct measure of V_θ . Figure 13 shows V_θ derived from these assumptions plotted against $\cos(\ell - \theta)$. The five clouds with the lowest values of $\cos(\ell - \theta)$ give similar results for V_θ which we will adopt as its most likely value, 240 km s^{-1} , indicated by a horizontal line in Figure 13.

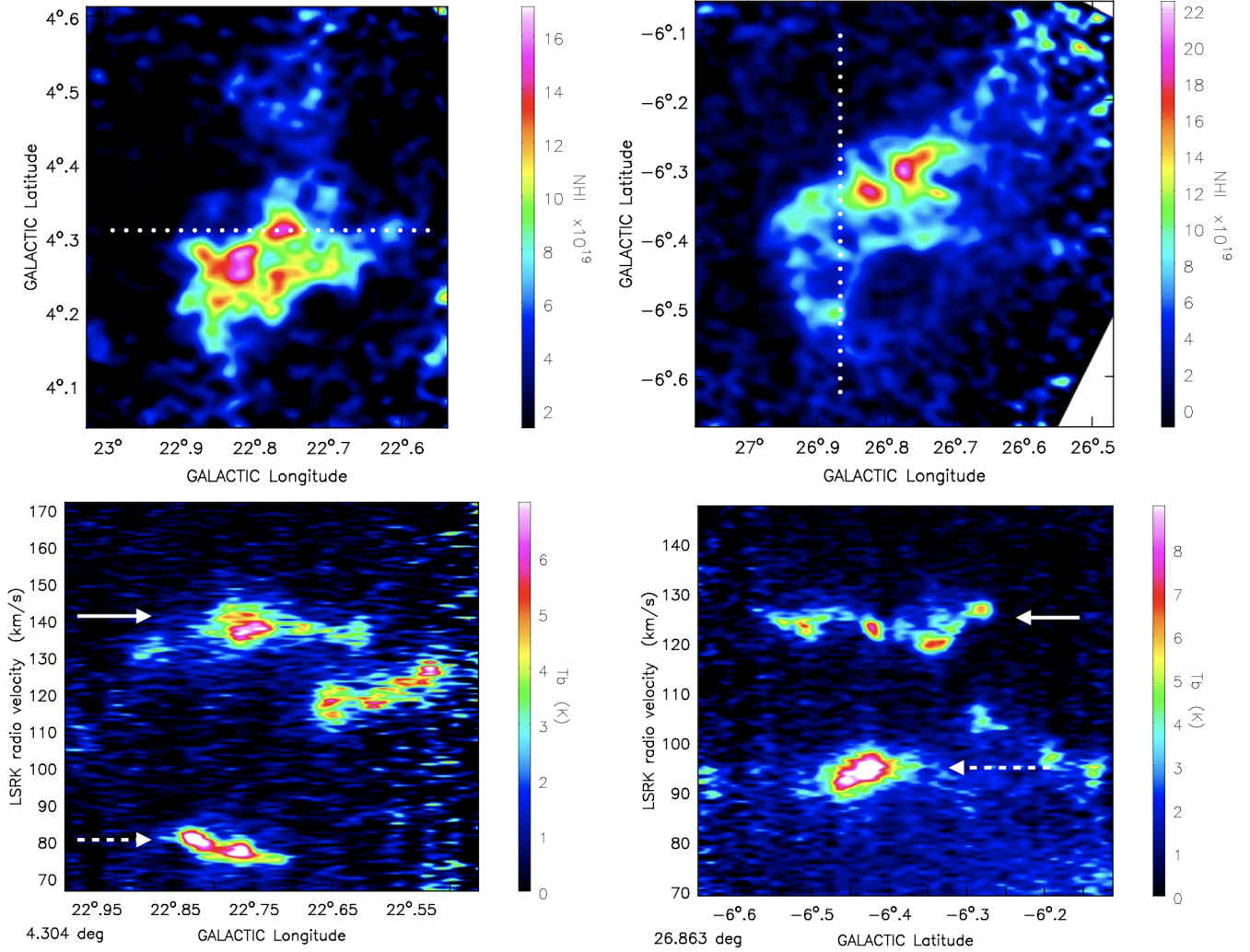


Figure 10. *Top panels:* High angular resolution images of the total N_{HI} from the P2015 data for two of the leading clouds observed in that survey: $22.74+4.30$ (left) and $26.84-6.38$ (right). *Bottom:* Cuts through the clouds in longitude-velocity ($22.74+4.30$, left) and latitude-velocity ($26.84-6.38$, right) along the directions given by dotted lines in the upper panels. The leading clouds are marked with a solid arrow and a dashed arrow identifies the Milky Way disk gas with which they are interacting. Unlike the examples in Figure 8, these data do not show kinematic bridges between the clouds and Milky Way gas. Instead, we derive evidence of interaction from the high degree of spatial coincidence between the gas at forbidden and permitted velocities, coincidence which is not seen in P2015 clouds except for those that are part of the Leading Component. The velocity of the interacting gas is used to derive a kinematic distance to the interaction.

For a constant $V_{\theta} = 240 \text{ km s}^{-1}$, and, assuming that $V_z \sin(b)$ is small close to the Galactic plane, Equation 1 can be solved for the V_R of the leading clouds. The results are shown in Figure 14 where the median value, 65 km s^{-1} , is indicated by a horizontal line. The error bars show the effect of a 10 km s^{-1} change in V_{θ} .

In principle, having estimates for V_{θ} and V_R should allow estimation of V_z for each cloud, but the determination is not robust, as $\sin(b)$ for these clouds is so small. Figure 15 shows $V_z \sin(b)$ vs. latitude with expectations for $V_z = \pm 100 \text{ km s}^{-1}$. The small values and large uncertainties suggest that V_z cannot be determined reliably so close to the Galactic Plane. The morphology and kinematics of the Smith Cloud indicate that its motion is to higher Galactic latitude, which requires $V_z > 0$. If the leading clouds share this motion they should have $V_z \sin(b) < 0$ at $b < 0$ and lie along a curve like the one marked by the plus signs.

The estimated values for the space velocity of the Leading Component clouds are compared with these for the Smith Cloud from L08 in Table 4. They are generally consistent.

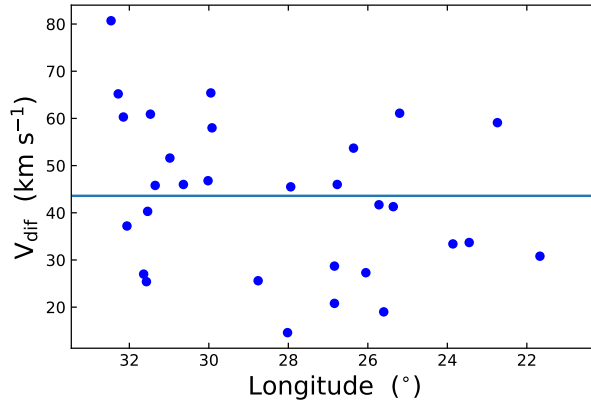


Figure 11. The line-of-sight velocity difference V_{dif} between the leading clouds and interacting gas, plotted against longitude. The median value is 44 km s^{-1} , and this is the best estimate of the line-of-sight deviation of the leading clouds from circular rotation at their location.

The total space velocity of the Leading Component clouds is $V_{\text{tot}} > 250 \text{ km s}^{-1}$ where the inequality indicates that we are unable to establish a reliable value for V_z . The Leading Clouds have a median line-of-sight velocity excess of 44 km s^{-1} with respect to the disk gas at their location. This is in the direction of Galactic rotation. As gas is stripped from these clouds (Figure 8) it adds not only mass but angular momentum to the disk.

6. WHAT IS THE LEADING COMPONENT?

In this paper we have presented arguments for the existence of an organized interstellar structure whose orientation and kinematics are not consistent with Galactic rotation, but which has a connection to the Smith high velocity cloud. The principle evidence for these claims is

1. A band of HI emission crossing the Galactic plane a few degrees ahead of the Smith Cloud with an orientation identical to that of the Smith Cloud.
2. The clouds in this structure have velocities larger than allowed by Galactic rotation (Figure 7) but the velocities are virtually identical to the V_{GSR} of the Smith Cloud, indicating that there is a kinematic as well as a spatial connection between the structures.
3. Many of the leading clouds are interacting with material at permitted velocities, confirming their peculiar kinematics (Figure 8 and Figure 11).

We thus believe that the Leading Component is an anomalous feature of the ISM related to the Smith Cloud, and despite its location in the Galactic plane this material had its origin as a high velocity cloud.

Evidence of interaction with normal disk gas allows us to estimate that where the Leading Component crosses the Galactic plane near longitude 25° it is 9.5 kpc from the Sun and 4.5 kpc from the Galactic Center. This is a region of the Galaxy with significant star formation activity as indicated by the presence of numerous HII regions (Anderson et al. 2012), some of which have a parallactic distance identical to the median kinematic distance to the Leading Component (Sato et al. 2014). The Leading Component has a neutral hydrogen mass comparable to that of the Smith Cloud, and it extends $\approx 17^\circ$ across the sky which, for our derived distance, makes its linear size $\sim 3 \text{ kpc}$, identical to that of the Smith Cloud.

From estimates of interaction locations we derive the velocity components for the leading clouds and find that they are similar to those of the Smith Cloud (Table 4). Because the two objects have a similar V_{GSR} (Figure 6) the similarity of the individual velocity components is not surprising, but is nonetheless reassuring that we are observing a single phenomenon. There is a gap between the Leading Component and the Smith Cloud of about 4° in which there is no strong emission that can be associated with either object (see the left panel of Figure 2). This would correspond to a gap of 0.6 - 1.6 kpc depending on the projection and assumed distance of the clouds.

The total space velocity of the Leading Component is $> 250 \text{ km s}^{-1}$, where the limit reflects our inability to measure V_z accurately. This is comparable to the L08 determination for the Smith Cloud of $V_{\text{tot}} = 296 \pm 20 \text{ km s}^{-1}$. There is

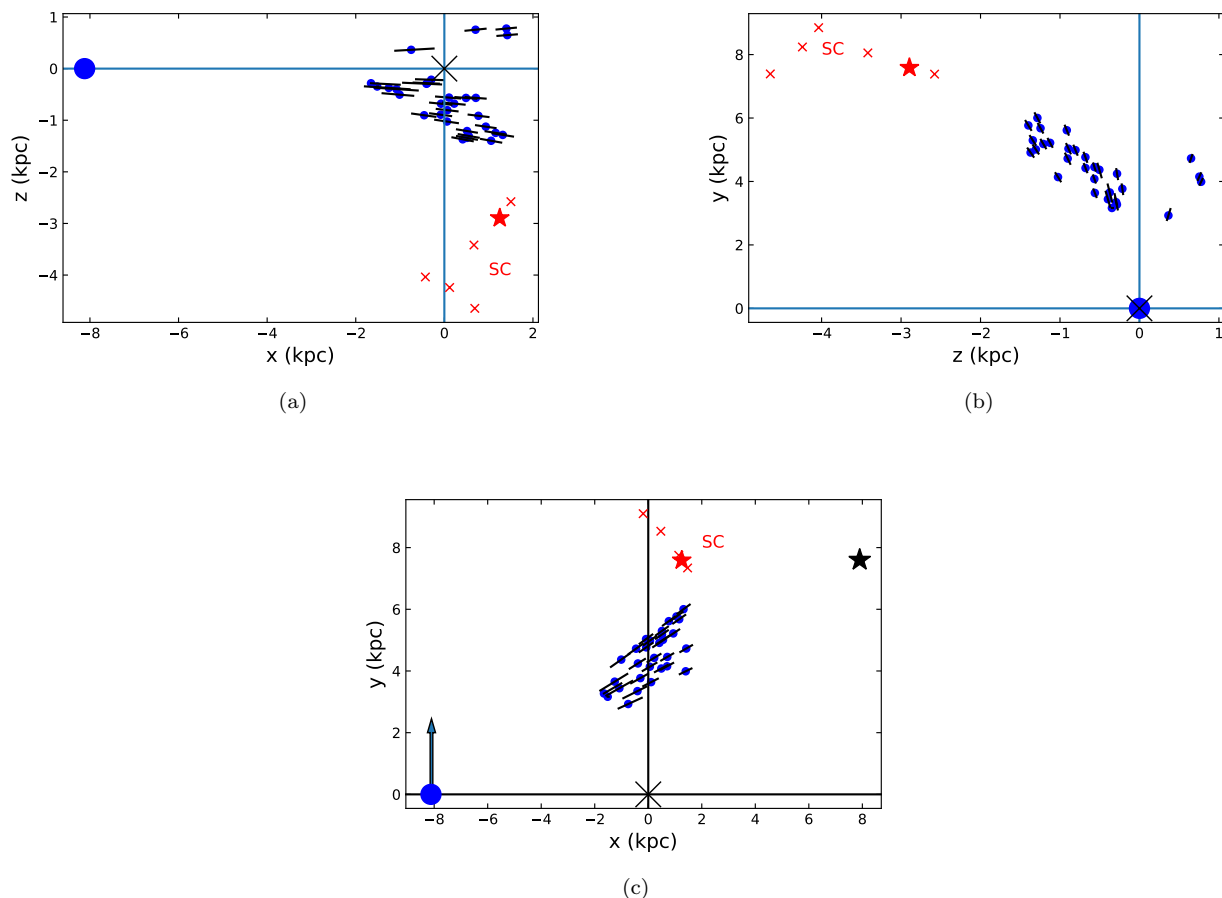


Figure 12. Location of regions where the leading clouds appear to be interacting with disk gas (small blue circles). These were derived for the PM rotation curve with error bars showing the effect of a $\pm 5 \text{ km s}^{-1}$ change in V_{GSR} . Red star and crosses are components of the Smith Cloud (SC) assuming a constant distance from the Sun for this object of 12.4 kpc. The large blue circle is at the position of the Sun and the “x” shows the Galactic center. (a) Projection of the cloud interaction locations on the x - z plane where x is in the direction of the Galactic Center (which is at 0,0), and z is distance from the Galactic plane. (b) Projection of cloud interaction locations on the z - y plane, where y is perpendicular to the line of sight from the Sun to the Galactic Center. To some extent the correlated structure in this panel simply reflects the alignment of the Leading Component with the Smith Cloud in longitude and latitude. (c) Cloud interaction locations in the x - y plane, which lies in the plane of the Milky Way. The black star shows the position of the Smith Cloud where it is projected to cross the Galactic plane in 27 Myr from the trajectory given in L08. The sense of Galactic rotation is indicated by the arrow extending upwards from the symbol for the Sun.

no information to suggest that either object has a velocity capable of escaping the Galaxy. The estimates of cloud space velocity from section 5 required several approximations; a more complete study of the entire Smith Cloud and Leading Component taking into account the Galactic potential and dynamical effects is in progress.

The Smith Cloud has been analyzed as an isolated system, perhaps the baryonic component of a dark matter subhalo (Nichols & Bland-Hawthorn 2009; Nichols et al. 2014; Tepper-García & Bland-Hawthorn 2018), and the question of the survival of its gaseous component given its strong interaction with the Milky Way’s circumgalactic medium has received considerable attention (Gritton et al. 2014; Galyardt & Shelton 2016). The discovery of the Leading Component suggests that the Smith Cloud may not be an isolated object but instead the more prominent manifestation of a system that stretches over more than 7 kpc on the sky with a gap between its two parts. It is interesting that “chains” of infalling gas occur naturally in some simulations that include simultaneous infall and outflow – cloud chains that may survive to pass through a galaxy’s disk (Melso et al. 2019). Perhaps that is what we

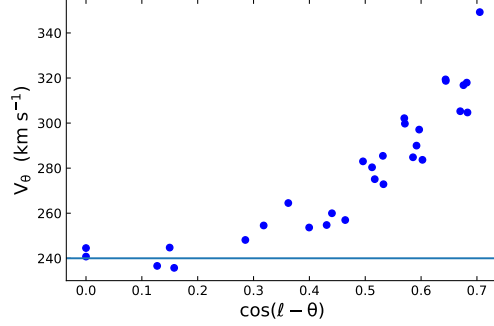


Figure 13. Derived values of V_θ as a function of $\cos(\ell - \theta)$ for $V_R = 0$, assuming that so close to the Galactic plane $V_z \sin(b) = 0$. For very low values of $\cos(\ell - \theta)$ any V_R component will be projected across the line of sight and V_{GSR} will be a function of V_θ alone (Equation 1). The horizontal line shows the adopted $V_\theta = 240 \text{ km s}^{-1}$.

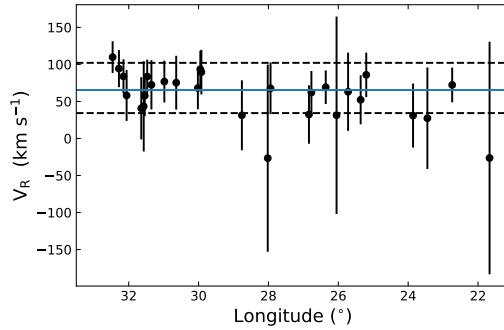


Figure 14. Derived values of V_R for $V_\theta = 240 \text{ km s}^{-1}$ assuming that so close to the Galactic Plane $V_z \sin(b) = 0$. The horizontal line shows the median value, 65 km s^{-1} . Error bars show the effect of changing V_θ by $\pm 10 \text{ km s}^{-1}$, and the dashed lines show the median values of V_R that result.

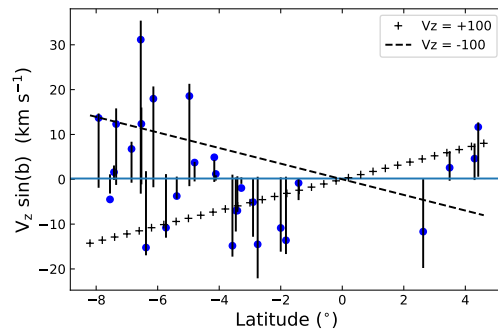


Figure 15. Derived values of $V_z \sin(b)$ for $V_\theta = 240 \text{ km s}^{-1}$ and $V_R = 65 \text{ km s}^{-1}$. The horizontal line shows the median value, 0.2 km s^{-1} . Error bars show the effect of changing the adopted V_θ by $\pm 10 \text{ km s}^{-1}$. The lines formed with dashes and plus signs show values expected for $V_z = -100 \text{ km s}^{-1}$ and $V_z = +100 \text{ km s}^{-1}$, respectively. The small values of the derived $V_z \sin(b)$ imply that V_z cannot be determined accurately from these data.

are observing here. If the metallicity of the Leading Component is similar to that of the Smith Cloud at ≈ 0.5 solar, it will lower the average metallicity of disk gas over the region of interaction.

In Lockman et al. (2008) and subsequent publications there was speculation about the future of the Smith Cloud, as its trajectory indicated that it would enter and merge with the Milky Way disk in a few tens of Myr perhaps triggering

a burst of star formation (Alig et al. 2018). Given the existence of the Leading Component it appears that the merger is already underway.

Acknowledgments The Green Bank Observatory is a facility of the National Science Foundation, operated by Associated Universities, Inc. The observations were made under GBT proposal codes 06C_038, 08A_014, and 09A_007. We thank E.C. Kornacki for assistance with the data reduction and the anonymous referee for useful comments. ECK, NP, and CT were supported by the NSF REU programs at the National Radio Astronomy Observatory and the Green Bank Observatory. FJL acknowledges the influence of the classic work by Toomre (1977) on the opening sentence of this paper.

Facilities: GBT

REFERENCES

- Alig, C., Hammer, S., Borodatchenkova, N., Dobbs, C. L., & Burkert, A. 2018, *ApJL*, 869, L2, doi: [10.3847/2041-8213/aaf1cb](https://doi.org/10.3847/2041-8213/aaf1cb)
- Anderson, L. D., Bania, T. M., Balser, D. S., & Rood, R. T. 2012, *ApJ*, 754, 62, doi: [10.1088/0004-637X/754/1/62](https://doi.org/10.1088/0004-637X/754/1/62)
- Barger, K. A., Nidever, D. L., Huey-You, C., et al. 2020, *ApJ*, 902, 154, doi: [10.3847/1538-4357/abb376](https://doi.org/10.3847/1538-4357/abb376)
- Betti, S. K., Hill, A. S., Mao, S. A., et al. 2019, *ApJ*, 871, 215, doi: [10.3847/1538-4357/aaf886](https://doi.org/10.3847/1538-4357/aaf886)
- Binney, J., & Fraternali, F. 2012, in *European Physical Journal Web of Conferences*, Vol. 19, European Physical Journal Web of Conferences, 08001, doi: [10.1051/epjconf/20121908001](https://doi.org/10.1051/epjconf/20121908001)
- Bish, H. V., Werk, J. K., Peek, J., Zheng, Y., & Putman, M. 2021, *ApJ*, 912, 8, doi: [10.3847/1538-4357/abeb6b](https://doi.org/10.3847/1538-4357/abeb6b)
- Bland-Hawthorn, J., Veilleux, S., Cecil, G. N., et al. 1998, *MNRAS*, 299, 611, doi: [10.1046/j.1365-8711.1998.01902.x](https://doi.org/10.1046/j.1365-8711.1998.01902.x)
- Boothroyd, A. I., Blagrove, K., Lockman, F. J., et al. 2011, *A&A*, 536, A81, doi: [10.1051/0004-6361/201117656](https://doi.org/10.1051/0004-6361/201117656)
- Brand, J., & Blitz, L. 1993, *A&A*, 275, 67
- Braun, R., & Thilker, D. A. 2004, *A&A*, 417, 421, doi: [10.1051/0004-6361:20034423](https://doi.org/10.1051/0004-6361:20034423)
- Burton, W. B. 1971, *A&A*, 10, 76
- . 1988, in *Galactic and Extragalactic Radio Astronomy*, ed. K. I. Kellermann & G. L. Verschuur, 295–358
- Celnik, W., Rohlfs, K., & Braunsfurth, E. 1979, *A&A*, 76, 24
- Eilers, A.-C., Hogg, D. W., Rix, H.-W., & Ness, M. K. 2019, *ApJ*, 871, 120, doi: [10.3847/1538-4357/aaf648](https://doi.org/10.3847/1538-4357/aaf648)
- Fox, A. J., Lehner, N., Lockman, F. J., et al. 2016, *ApJL*, 816, L11, doi: [10.3847/2041-8205/816/1/L11](https://doi.org/10.3847/2041-8205/816/1/L11)
- Fraternali, F. 2017, in *Astrophysics and Space Science Library*, Vol. 430, Gas Accretion onto Galaxies, ed. A. Fox & R. Davé, 323, doi: [10.1007/978-3-319-52512-9_14](https://doi.org/10.1007/978-3-319-52512-9_14)
- Galyardt, J., & Shelton, R. L. 2016, *ApJL*, 816, L18, doi: [10.3847/2041-8205/816/1/L18](https://doi.org/10.3847/2041-8205/816/1/L18)
- Gravity Collaboration, Abuter, R., Amorim, A., et al. 2018, *A&A*, 615, L15, doi: [10.1051/0004-6361/201833718](https://doi.org/10.1051/0004-6361/201833718)
- Gritton, J. A., Shelton, R. L., & Kwak, K. 2014, *ApJ*, 795, 99, doi: [10.1088/0004-637X/795/1/99](https://doi.org/10.1088/0004-637X/795/1/99)
- Heitsch, F., Marchal, A., Miville-Deschênes, M. A., Shull, J. M., & Fox, A. J. 2022, *MNRAS*, 509, 4515, doi: [10.1093/mnras/stab3266](https://doi.org/10.1093/mnras/stab3266)
- Henley, D. B., Gritton, J. A., & Shelton, R. L. 2017, *ApJ*, 837, 82, doi: [10.3847/1538-4357/aa5df7](https://doi.org/10.3847/1538-4357/aa5df7)
- HI4PI Collaboration, Ben Bekhti, N., Flöer, L., et al. 2016, *A&A*, 594, A116, doi: [10.1051/0004-6361/201629178](https://doi.org/10.1051/0004-6361/201629178)
- Hill, A. S., Haffner, L. M., & Reynolds, R. J. 2009, *ApJ*, 703, 1832, doi: [10.1088/0004-637X/703/2/1832](https://doi.org/10.1088/0004-637X/703/2/1832)
- Hill, A. S., Mao, S. A., Benjamin, R. A., Lockman, F. J., & McClure-Griffiths, N. M. 2013, *ApJ*, 777, 55, doi: [10.1088/0004-637X/777/1/55](https://doi.org/10.1088/0004-637X/777/1/55)
- Kalberla, P. M. W., Burton, W. B., Hartmann, D., et al. 2005, *A&A*, 440, 775, doi: [10.1051/0004-6361:20041864](https://doi.org/10.1051/0004-6361:20041864)
- Lehner, N., Howk, J. C., Marasco, A., & Fraternali, F. 2022, *MNRAS*, 513, 3228, doi: [10.1093/mnras/stac987](https://doi.org/10.1093/mnras/stac987)

Table 1. Leading clouds detected in the GBT Observations. Columns as follow: (1) Galactic longitude; (2) Galactic latitude; (3) Maximum line brightness temperature; (4) LSR velocity; (5) Line width FWHM; (6) Maximum HI column density; (7) observed angular size FWHM; (8) position angle with respect to the Galactic pole; (9) HI mass assuming a distance of 10 kpc. Columns (3)-(5) are from a Gaussian fit. Column (7) is from a 2D Gaussian fit to the channel map at the velocity of peak emission and is not corrected for beam smearing. Column (9) is calculated assuming a distance from the Sun of 10 kpc. Uncertainties are propagated from the error associated with the Gaussian fits. If a cloud shows evidence that it is interacting with normal gas in the Milky Way disk the velocity of that gas is given as V_{MW} in column (10).

ℓ	b	T_{pk}	V_{LSR}	FWHM	N_{HI}	Θ_{obs}	PA	M_{HI} (10 kpc)	V_{MW}
($^{\circ}$)	($^{\circ}$)	(K)	(km s^{-1})	(km s^{-1})	(10^{19} cm^{-2})	($'$)	($^{\circ}$)	(M_{\odot})	(km s^{-1})
(1)	(2)	(3)	(4)	(5)	(6)	(7)	(8)	(9)	(10)
21.67	+2.63	2.41±0.05	149.6±0.3	18.9±0.8	8.8	—	—	5.6e+03	119
22.74	+4.30	3.48±0.04	137.3±0.1	11.0±0.2	7.5	17.9×15.0	125±6	1.2e+03	78
23.45	-2.00	1.84±0.04	146.2±0.1	12.3±0.3	4.4	—	—	2.4e+03	112
23.86	-3.57	1.83±0.03	136.6±0.2	19.7±0.6	7.0	22.6×16.0	84±3	1.3e+03	103
25.15	-0.55	4.71±0.09	143.1±0.3	17.3±0.6	15.8	71.4×57.0	27±6	1.0e+04	—
25.20	+4.42	2.76±0.04	147.7±0.1	12.8±0.2	6.9	16.7×14.0	134±6	1.4e+03	87
25.36	-3.41	2.63±0.05	132.2±0.2	16.9±0.5	8.6	72.0×45.6	94±3	3.8e+03	91
25.60	-2.71	1.72±0.05	145.0±0.2	13.5±0.6	4.5	37.0×13.6	168±1	1.1e+03	126
25.72	-1.42	1.70±0.10	146.7±0.3	9.1±0.9	3.0	17.8×12.4	126±4	6.6e+02	105
25.74	+4.78	1.06±0.03	142.6±0.3	24.8±0.8	5.1	17.2×13.7	84±6	7.7e+02	—
26.05	-2.90	2.13±0.06	140.8±0.2	13.3±0.5	5.5	41.3×25.0	126±2	1.3e+03	114
26.36	+3.49	7.62±0.03	120.2±0.0	15.9±0.1	23.5	84.6×45.6	1±2	1.1e+04	66
26.77	-3.28	3.16±0.03	127.1±0.1	15.6±0.2	9.6	—	—	6.9e+03	81
26.84	-2.24	1.44±0.06	136.8±0.4	12.4±1.0	3.4	36.3×27.9	129±5	9.5e+02	116
26.84	-6.38	3.78±0.04	123.0±0.1	10.0±0.1	7.4	29.2×14.7	132±1	1.9e+03	94
27.94	-4.11	2.90±0.04	132.7±0.1	12.5±0.2	7.0	47.9×21.8	9±1	3.2e+03	87
28.02	-2.75	4.03±0.05	124.6±0.2	18.4±0.5	14.4	77.4×37.8	127±1	8.6e+03	110
28.76	-1.83	11.35±0.08	121.8±0.1	12.8±0.1	28.2	37.4×20.3	89±2	1.1e+04	96
29.29	-4.34	3.46±0.04	135.8±0.1	9.0±0.1	6.1	19.9×15.3	124±7	1.0e+03	—
29.31	-7.30	1.36±0.04	122.8±0.1	11.1±0.4	2.9	19.7×11.0	51±2	4.3e+02	—
29.36	-5.03	1.71±0.05	130.9±0.1	6.8±0.2	2.3	15.3×11.8	163±3	2.8e+02	—
29.92	-7.92	0.79±0.03	132.3±0.4	18.1±1.1	2.8	27.2×18.0	16±4	1.1e+03	74
29.95	-6.14	3.49±0.03	128.2±0.1	13.5±0.2	9.1	22.0×15.8	149±3	1.9e+03	63
30.02	-7.42	3.78±0.03	117.7±0.1	19.6±0.2	14.4	22.0×16.8	98±3	1.3e+03	71
30.07	-3.92	5.30±0.11	121.3±0.2	15.2±0.6	15.6	—	—	1.7e+03	—
30.37	-6.31	1.33±0.03	119.2±0.2	21.5±0.7	5.5	46.6×38.0	91±7	2.0e+03	—
30.64	-4.16	5.35±0.04	128.2±0.0	12.5±0.1	13.0	28.3×15.4	137±2	2.5e+03	82
30.98	-6.85	1.01±0.02	119.2±0.5	29.6±1.2	5.8	—	—	2.3e+03	68
31.35	-4.80	2.40±0.03	121.7±0.1	15.2±0.3	7.1	54.6×20.2	129±1	6.2e+02	76
31.47	-6.53	3.57±0.03	111.8±0.1	17.8±0.2	12.3	38.9×22.1	162±1	3.1e+03	51
31.54	-7.55	3.86±0.03	105.2±0.1	19.4±0.2	14.5	32.1×18.2	48±2	1.5e+03	65
31.57	-3.46	2.14±0.05	120.7±0.2	15.3±0.6	6.4	—	—	1.2e+03	95
31.64	-5.73	4.39±0.05	112.2±0.0	8.0±0.1	6.8	—	—	1.1e+03	85
32.04	-4.10	1.79±0.03	120.6±0.2	19.6±0.5	6.8	—	—	1.0e+03	—
32.06	-5.38	5.22±0.03	112.9±0.1	15.2±0.1	15.4	—	—	3.2e+03	76
32.15	-7.35	2.73±0.03	110.2±0.2	18.8±0.4	10.0	30.0×24.6	107±4	3.8e+03	50
32.28	-4.97	3.15±0.04	121.1±0.1	13.7±0.2	8.3	21.8×17.1	78±7	1.2e+03	56
32.46	-6.55	2.46±0.03	123.4±0.1	14.0±0.2	6.7	44.1×17.7	147±1	2.3e+03	43

Table 2. Leading cloud population properties. Distant-dependent quantities were calculated assuming a distance from the Sun, $d_{10} = 10$ kpc. Spectral properties were derived from a Gaussian fit at the location of the peak 21cm brightness. The quantity V_{GSR} was calculated using a Galactic circular velocity of 230 km s^{-1} at the location of the Sun. V_{dif} is the difference in velocity between the cloud and the material it appears to be interacting with. Angular sizes were derived from a Gaussian fit at the velocity of peak emission corrected by subtracting in quadrature the $10'$ effective angular resolution of the survey. Column (4) gives the number of clouds used to establish each quantity.

Property	Median	Range	n clouds
(1)	(2)	(3)	(4)
T_{pk} (K)	2.7	0.79 – 11.35	38
FWHM (km s^{-1})	15.2	6.8 – 29.6	38
Peak N_{HI} (10^{19} cm^{-2})	7.0	2.3 – 28.2	38
V_{GSR} (km s^{-1})	237	222 – 248	38
Θ_{maj} ($'$)	28.3	11.6 – 84	29
Θ_{min} ($'$)	15.0	4.6 – 56	29
PA ($^{\circ}$)	124	1 – 168	29
Diam (d_{10} pc)	57	25 – 183	29
n ($\text{cm}^{-3} d_{10}^{-1}$)	0.43	0.13 – 1.24	29
M_{HI} ($10^3 d_{10}^2 M_{\odot}$)	1.6	0.28 – 11.0	38
V_{dif} (km s^{-1})	44	15 – 81	30

Table 3. Properties of three leading component clouds observed by the GBT at $10'$ resolution and by P2015 at $1'$ resolution. The P2015 diameters refer to the cloud core and were scaled to a distance of 10 kpc.

Property	G22.74+4.30	G25.20+4.42	G26.84-6.38
	GBT, P2015	GBT, P2015	GBT, P2015
(1)	(2)	(3)	(4)
Peak N_{HI} (10^{20} cm^{-2})	0.75, 1.7	0.69, 1.6	0.74, 2.2
FWHM (km s^{-1}) ^a	11.0, 5.8/24.3	12.8, 13.4	10.0, 3.0/14.5
Diam (d_{10} pc)	37.5, 12.6	33.3, 13.3	50.0, 11.0
n ($\text{cm}^{-3} d_{10}^{-1}$)	0.65, 4.4	0.67, 3.9	0.48, 6.4
PA ($^{\circ}$)	125, 122	134, 156	132, 128

^aG22.74+4.30 and G26.84-6.38 have two spectral components in the P2015 data, one broad and one narrow.

Table 4. Space velocities of the Smith Cloud and the Leading Component. Smith Cloud entries are from the model in L08. Leading cloud entries are from the discussion in section 5 where the the uncertainty in V_R shows the effect of a 10 km s^{-1} change in the adopted V_θ , and V_z could not be determined.

Object	V_θ	V_R	V_z
	km s^{-1}	km s^{-1}	km s^{-1}
(1)	(2)	(3)	(4)
Smith Cloud	270 ± 21	94 ± 18	73 ± 26
Leading Component	240	65 ± 35	—

- Levine, E. S., Heiles, C., & Blitz, L. 2008, ApJ, 679, 1288, doi: [10.1086/587444](https://doi.org/10.1086/587444)
- Li, M., & Tonnesen, S. 2020, ApJ, 898, 148, doi: [10.3847/1538-4357/ab9f9f](https://doi.org/10.3847/1538-4357/ab9f9f)
- Lockman, F. J. 2003, ApJL, 591, L33, doi: [10.1086/376961](https://doi.org/10.1086/376961)
- Lockman, F. J., Benjamin, R. A., Heroux, A. J., & Langston, G. I. 2008, ApJL, 679, L21, doi: [10.1086/588838](https://doi.org/10.1086/588838)
- Lockman, F. J., Murphy, E. M., Petty-Powell, S., & Urick, V. J. 2002, ApJS, 140, 331, doi: [10.1086/339371](https://doi.org/10.1086/339371)
- Marasco, A., & Fraternali, F. 2017, MNRAS, 464, L100, doi: [10.1093/mnras/slw195](https://doi.org/10.1093/mnras/slw195)
- Marasco, A., Fraternali, F., Lehner, N., & Howk, J. C. 2022, MNRAS, 515, 4176, doi: [10.1093/mnras/stac1172](https://doi.org/10.1093/mnras/stac1172)
- Marinacci, F., Binney, J., Fraternali, F., et al. 2010, MNRAS, 404, 1464, doi: [10.1111/j.1365-2966.2010.16352.x](https://doi.org/10.1111/j.1365-2966.2010.16352.x)
- McClure-Griffiths, N. M., & Dickey, J. M. 2007, ApJ, 671, 427, doi: [10.1086/522297](https://doi.org/10.1086/522297)
- McClure-Griffiths, N. M., Staveley-Smith, L., Lockman, F. J., et al. 2008, ApJL, 673, L143, doi: [10.1086/528683](https://doi.org/10.1086/528683)
- Melso, N., Bryan, G. L., & Li, M. 2019, ApJ, 872, 47, doi: [10.3847/1538-4357/aafaf5](https://doi.org/10.3847/1538-4357/aafaf5)
- Mróz, P., Udalski, A., Skowron, D. M., et al. 2019, ApJL, 870, L10, doi: [10.3847/2041-8213/aaf73f](https://doi.org/10.3847/2041-8213/aaf73f)
- Muller, C. A., Oort, J. H., & Raimond, E. 1963, Academie des Sciences Paris Comptes Rendus, 257, 1661
- Nichols, M., & Bland-Hawthorn, J. 2009, ApJ, 707, 1642, doi: [10.1088/0004-637X/707/2/1642](https://doi.org/10.1088/0004-637X/707/2/1642)
- Nichols, M., Mirabal, N., Agertz, O., Lockman, F. J., & Bland-Hawthorn, J. 2014, MNRAS, 442, 2883, doi: [10.1093/mnras/stu1028](https://doi.org/10.1093/mnras/stu1028)
- Oort, J. H. 1969, Nature, 224, 1158, doi: [10.1038/2241158a0](https://doi.org/10.1038/2241158a0)
- Park, G., Koo, B.-C., Kang, J.-h., et al. 2016, ApJL, 827, L27, doi: [10.3847/2041-8205/827/2/L27](https://doi.org/10.3847/2041-8205/827/2/L27)
- Persic, M., Salucci, P., & Stel, F. 1996, MNRAS, 281, 27, doi: [10.1093/mnras/278.1.27](https://doi.org/10.1093/mnras/278.1.27)
- Pidopryhora, Y., Lockman, F. J., Dickey, J. M., & Rupen, M. P. 2015, ApJS, 219, 16, doi: [10.1088/0067-0049/219/2/16](https://doi.org/10.1088/0067-0049/219/2/16)
- Prestage, R. M., Constantikes, K. T., Hunter, T. R., et al. 2009, IEEE Proceedings, 97, 1382, doi: [10.1109/JPROC.2009.2015467](https://doi.org/10.1109/JPROC.2009.2015467)
- Putman, M. E. 2017, in Astrophysics and Space Science Library, Vol. 430, Gas Accretion onto Galaxies, ed. A. Fox & R. Davé, 1, doi: [10.1007/978-3-319-52512-9_1](https://doi.org/10.1007/978-3-319-52512-9_1)
- Putman, M. E., Bland-Hawthorn, J., Veilleux, S., et al. 2003, ApJ, 597, 948, doi: [10.1086/378555](https://doi.org/10.1086/378555)
- Putman, M. E., Peek, J. E. G., & Joung, M. R. 2012, ARA&A, 50, 491, doi: [10.1146/annurev-astro-081811-125612](https://doi.org/10.1146/annurev-astro-081811-125612)
- Putman, M. E., Saul, D. R., & Mets, E. 2011, MNRAS, 418, 1575, doi: [10.1111/j.1365-2966.2011.19524.x](https://doi.org/10.1111/j.1365-2966.2011.19524.x)
- Reid, M. J., Menten, K. M., Brunthaler, A., et al. 2014, ApJ, 783, 130, doi: [10.1088/0004-637X/783/2/130](https://doi.org/10.1088/0004-637X/783/2/130)
- Richter, P. 2017, in Astrophysics and Space Science Library, Vol. 430, Gas Accretion onto Galaxies, ed. A. Fox & R. Davé, 15, doi: [10.1007/978-3-319-52512-9_2](https://doi.org/10.1007/978-3-319-52512-9_2)
- Sato, M., Wu, Y. W., Immer, K., et al. 2014, ApJ, 793, 72, doi: [10.1088/0004-637X/793/2/72](https://doi.org/10.1088/0004-637X/793/2/72)
- Smith, G. P. 1963, BAN, 17, 203
- Sofue, Y., Kudoh, T., Kawamura, A., Shibata, K., & Fujimoto, M. 2004, PASJ, 56, 633, doi: [10.1093/pasj/56.4.633](https://doi.org/10.1093/pasj/56.4.633)
- Stark, D. V., Baker, A. D., & Kannappan, S. J. 2015, MNRAS, 446, 1855, doi: [10.1093/mnras/stu2182](https://doi.org/10.1093/mnras/stu2182)

- Tepper-García, T., & Bland-Hawthorn, J. 2018, MNRAS, 473, 5514, doi: [10.1093/mnras/stx2680](https://doi.org/10.1093/mnras/stx2680)
- Thilker, D. A., Braun, R., Walterbos, R. A. M., et al. 2004, ApJL, 601, L39, doi: [10.1086/381703](https://doi.org/10.1086/381703)
- Toomre, A. 1977, ARA&A, 15, 437, doi: [10.1146/annurev.aa.15.090177.002253](https://doi.org/10.1146/annurev.aa.15.090177.002253)
- Wakker, B. P., & van Woerden, H. 1991, A&A, 250, 509
- . 1997, ARA&A, 35, 217, doi: [10.1146/annurev.astro.35.1.217](https://doi.org/10.1146/annurev.astro.35.1.217)
- Wakker, B. P., York, D. G., Wilhelm, R., et al. 2008, ApJ, 672, 298, doi: [10.1086/523845](https://doi.org/10.1086/523845)
- Westmeier, T., Brüns, C., & Kerp, J. 2008, MNRAS, 390, 1691, doi: [10.1111/j.1365-2966.2008.13858.x](https://doi.org/10.1111/j.1365-2966.2008.13858.x)
- Wolfe, S. A., Lockman, F. J., & Pisano, D. J. 2016, ApJ, 816, 81, doi: [10.3847/0004-637X/816/2/81](https://doi.org/10.3847/0004-637X/816/2/81)
- Zheng, Y., Putman, M. E., Peek, J. E. G., & Joung, M. R. 2015, ApJ, 807, 103, doi: [10.1088/0004-637X/807/1/103](https://doi.org/10.1088/0004-637X/807/1/103)